

XMM-Newton X-Ray Spectroscopy of the B2 Bright Giant ϵ Canis Majoris

Geneviève de Messières

Swarthmore College

gdemess1@swarthmore.edu

ABSTRACT

How do hot stars produce X-rays? The two major theories involve radiatively driven wind shocks or magnetic coronal heating. We have acquired a high-resolution spectrum of the nearby B giant ϵ Canis Majoris, from the Reflection Grating Spectrometer instrument of the *XMM-Newton* space telescope. Due to its brightness, ϵ CMa provides a valuable opportunity to test these theories. We fit emission lines from the spectrum in order to draw conclusions about the conditions of velocity and height under which X-rays were generated. The emission lines indicate that the X-ray-emitting plasma has an average speed of 162 km s^{-1} . Analysis of helium-like F/I ratios yields a radius of emission between 1 and $2.1 R_*$. Characteristic plasma temperatures from a global fit are between 2 and 6 MK.

1. Introduction

1.1. X-ray production on hot stars

For several decades there have been two major theories of X-ray production on O and B stars: coronal heating, and radiatively driven wind shocks (Cohen et al. 1996).

The first theory is that the X-rays are produced in the corona, near the surface of the star. Coronal heating requires the presence of a variable magnetic field, which is not predicted on an evolved hot star. Hot stars have more efficient radiative transfer than the Sun, and are not expected to have convection in their envelopes. Therefore, our understanding is that a hot star would not have a complex, small-scale magnetic field threaded through its photosphere such as the one generated by the Sun's magnetic dynamo. A hot star could retain a primordial magnetic field, spanning the diameter of the star, from the time of its birth. However, without a dynamo to sustain it, the field would be shed over time, and would dissipate by the time the star reaches the giant stage, even for a short-lived star.

Coronal heating theory makes definite predictions about emission line profiles. Our current understanding of coronal heating on the Sun involves closed magnetic loops and arches, hundreds of thousands of kilometers high, which contain heated plasma (Culhane 2001). Interaction between two loops or between a loop and a larger magnetic structure can cause magnetic reconnection, and the conversion of magnetic energy into thermal energy. Emission in the corona occurs on or close to the surface of the star. Emission lines generated by coronally heated material are expected to be narrow because of the lack of fast net outward flow.

The second theory is that the X-rays are produced by shocks in a radiatively accelerated stellar wind (Lamers & Cassinelli 1999). A photon absorbed by an ion in the stellar wind transfers its momentum to the particle before it is re-emitted in a random direction. The peak of radiation for a luminous hot star is in the

ultraviolet, where there are many absorption lines in the star's outer envelope. The wind can be accelerated to thousands of kilometers per second, within a few stellar radii of the surface. The wind of a $10R_{\odot}$ star can be accelerated to its terminal velocity of 2000 km s^{-1} in 10^4 seconds, with about 10^7 photons scattering off each ion per second (Lamers & Cassinelli 1999).

It is possible for the wind to be efficiently accelerated even if it is transparent to all but a few wavelengths, corresponding to the energy of certain line transitions. An ion at the base of the wind absorbs a photon at some line transition wavelength, where the blackbody luminosity of the star is strong. O and early B type stars, with a range in surface temperatures from about 50 to 20 kK, have the peak of their emission in the ultraviolet, between 1450 and 580 Å. The photon is re-emitted, and the ion is accelerated away from the star. Before long, the ion is shadowed at that wavelength by the ions closer to the star, which are also being accelerated at the same line transition. The light from the star, however, is redshifted relative to the ion. The ion is now transparent to the light at the wavelength that originally accelerated it, and opaque to a narrow band of light at a slightly bluer wavelength. The blue wavelength has not been absorbed by any other ions further down in the wind. By the line driving mechanism, the star can accelerate its wind using wide bands of its spectrum, rather than only a few narrow absorption lines (Lamers & Cassinelli 1999).

Instabilities in the acceleration cause collisions between fast and slow moving shells of the wind. If the fast shell is moving faster than the local speed of sound, the front between the fast shell and the slow shell is discontinuous in density and velocity. At this shock front, the wind is heated. A wind shock source is moving radially outward, so its emission lines are, in general, broadened. The shocks are typically generated in the range $1.5 - 7R_{*}$ (Feldmeier 1995).

2. The star, ϵ Canis Majoris

2.1. Stellar properties

ϵ Canis Majoris, a B2 bright giant also known as Adara, lies in a tunnel of evacuated interstellar gas (Gry & Jenkins 2001). It is the brightest star in the sky in the extreme ultraviolet. It has been optically resolved with the Narrabri interferometer (Hanbury Brown et al. 1974), and its parallax has been determined. Aside from the EUV excess, it appears to be a typical B giant. There has been no evidence that it has a magnetic field, and its moderately strong stellar wind has been observed (Cohen et al. 1996).

2.2. B stars

ϵ Canis Majoris is a popular subject for study because of its proximity and the lack of interstellar absorption. It has previously been studied by *ROSAT*, *EUVE*, *IUE*, and by other telescopes down to the infrared band (Cassinelli et al. 1995). The *XMM-Newton* observation is the first high-resolution X-ray observation of ϵ CMa. Furthermore, most X-ray studies of B stars have been done under low resolution. Recently, high-resolution spectra of τ Scorpii, a young B0.2 V star, and γ Cassiopeia, a B0.5e star, have been analyzed using high-resolution Chandra spectroscopy.

ϵ CMa is a candidate to become a template for future models for B stars. ζ Puppis is the usual template for hot stars. τ Scorpii is a popular B star target, with an intermediate temperature, but it is generally acknowledged to be an unusual star because of its extreme youth. Finding an average B star whose spectrum we can study in detail is important in the X-ray band because there are not very many strong, nearby hot

Table 1. Stellar Properties

| Parameters | Value |
|------------------|--|
| Spectral type | B1.5 II ^a |
| m_v | 1.5 ^a |
| Distance | 132 ± 10 pc ^{b,c} |
| T_{eff} | 20990 ± 760 K ^d |
| R_* | $11.3 \pm 1.4 R_{\odot}$ ^{e,f} |
| \dot{M} | $1 \times 10^{-8} M_{\odot} \text{yr}^{-1}$ ^g |
| v_{∞} | 910 km s^{-1} ^h |
| $V \sin i$ | 25 km s^{-1} ⁱ |

^aWalborn & Fitzpatrick (1997)

^bThe distance in parsecs is given by $(1\text{AU})/(7.57 * 10^{-3} \text{''})$.

^cParallax = 7.57 ± 0.57 mas (Hipparcos Main Catalogue)

^dCode et al. (1975)

^e $R_* = d \times \theta_d / 2000$. Convert from AU into R_* by a factor of 214.9.

^f $\theta_d = 0.80 \pm 0.05$ mas. (Hanbury Brown et al. 1974)

^gGregorio et al. (2002)

^hCohen et al. (1996)

ⁱAbt, Levato & Grosso (2002). No uncertainties are given.

stellar X-ray sources. We need strong, high resolution spectra which we can test our models against, so we can extrapolate those models to fainter sources. It is also valuable to compare high-resolution spectra of O and B stars because of the sharp drop in wind strength between the two categories (Cohen, Cassinelli, & MacFarlane 1997).

3. Observations

We observed ϵ CMa in March, 2001, for a total of close to 55 ks using the Reflection Grating Spectrometer (RGS). Figure 1 represents the first order of the two RGS instruments. The second order contains enough data that we used it to refine the fits to some of the emission lines.

There is no way to combine the second, shorter observation with the first to make a single, long observation. Therefore, we used only the longer observation for most of our fits. We found that for strong lines, fitting the two observations simultaneously reduced the extent of the confidence intervals. For weak lines, there is no benefit to using the second observation in the fit.

The continuum of the spectrum is weak and is probably due to bremsstrahlung radiation. The emission lines of an optically thick shocked wind are not Gaussian but skewed and flat-topped (Owocki & Cohen 2001), but this profile approximates a Gaussian for optically thin winds. For example, ζ Puppis is an O star with a mass loss rate of about $5 \times 10^6 M_{\odot} \text{yr}^{-1}$, a hundred times as strong as ϵ CMa's. ζ Pup has broad emission line profiles which are not Gaussian, but could be approximated as almost Gaussian in shape (Kramer 2003). We expect low densities in the wind of ϵ CMa and low wind opacity. Furthermore, the emission line profiles are not visibly skewed, so we chose to use Gaussian models for simplicity.

3.1. The Reflection Grating Spectrometer spectrum

The Reflection Grating Spectrometer units, composed of Reflection Grating Assemblies (RGAs) and RGS Focal Cameras (RFCs), have a peak effective area of 140 cm^2 at 15 \AA (Kahn et al. 2001). The RGAs, located on two of *XMM-Newton*'s three telescopes, collect about 58% of the light focused by the mirrors (Ehle et al 2003). There are nine MOS CCD chips on each RFC.

The resolution of the RGS instruments is defined on the range of 7 to 35 \AA for first order, and 7 to 18 \AA for the second order (Ehle et al 2003).

The RGS 1 first order has half width half max (HWHM) resolution of about $\Delta\lambda = 0.03 \text{ \AA} = 1300 \text{ km s}^{-1}$ at $\lambda = 7 \text{ \AA}$, and $0.035 \text{ \AA} = 300 \text{ km s}^{-1}$ at 35 \AA . The resolution function is approximately linear between these points. The RGS 2 first order has HWHM resolution of about 0.035 \AA across the range. Then, the resolution at 20 \AA is 450 km s^{-1} for the first order, and 525 km s^{-1} for the second order. The RGS 1 second order has resolution of about 0.015 \AA , and about 0.02 \AA for the RGS 2 second order. At 20 \AA , these orders have resolution of 225 and 300 km s^{-1} , respectively.

3.2. Data reduction

We reduced the spectra using the SAS 5.4 software package. We filtered three solar flares out of the longer observation, using a rate cutoff of $0.2 \text{ counts s}^{-1}$. A long solar flare contaminates the shorter observation,

but we found that when we use the second observation in a fit, we obtained narrower confidence intervals when using the unfiltered observation. Filtering out the long flare eliminates too much of the useful data.

The background file for each spectrum is maintained separately from the total spectrum file. We did not create a spectrum file that was background-subtracted, because that would invalidate the Poisson distribution of the data (Arnaud 1996). Instead, we input both the spectrum file and the background file into XSPEC v.11.2.0, our primary data analysis program. We fit a background model to both the background file and spectrum file simultaneously, and added other models (such as Gaussian, bremsstrahlung, and APEC models; see Sections 4.2 and 4.3) to the fit for the spectrum file. This method permitted us to correct for the background and retain a well-defined statistic.

4. Data Analysis

4.1. Statistics

It was necessary to bin our spectrum to reduce noise, but we chose to use criteria that resulted in fine binning: each bin had to contain at least one count. We tested these spectra against a coarsely binned set, with at least 20 counts per bin, and found that the coarse binning produces an equally good fit for a strong line. However, spectral detail is lost, so for weaker or blended lines, the coarse binning is inferior.

The χ^2 statistic requires a Gaussian distribution of counts per bin, so it does not accurately describe a finely binned spectrum. The distribution of counts per bin for a finely binned spectrum is Poisson, and the Cash statistic is the maximum likelihood statistic for the Poisson distribution. Therefore, when making models to the spectra, we varied the parameters until the Cash statistic was minimized, to find the best fit (Kramer 2003).

The Cash statistic applies only to pure Poisson distributions, so it is not accurate if the data has been previously background-subtracted, or has a systematic error. In XSPEC we work with a total spectrum and its background spectrum in parallel, however, rather than working with a spectrum which has its background already subtracted (see Section 3.2).

To determine the uncertainties of a best fit, we used the "steppar" procedure in XSPEC to find the confidence interval: the region in parameter space where the C-statistic does not increase by more than a certain interval. We are interested in the 68% likelihood confidence interval, where the Cash statistic increases by no more than 2.3 (Arnaud 1996).

Unlike χ^2 , the C-statistic does not have an objective measure of goodness of fit. The minimum values of the Cash statistic cannot be compared between two different fits (different spectra, range of data, model types, etc) to determine which is better. Two minimum values of the C-statistic can only be compared between different fits for the same range of the same spectrum with the same bins, using the same model. A fit with smaller confidence intervals is typically superior, but we found that this is not an absolute determination.

For example, we compared a fit of a single emission line using the finely binned spectrum, under the Cash statistic, to a fit of the same line using a coarsely binned spectrum, under the χ^2 statistic. The results for the coarsely binned spectrum often returned a narrower confidence region, but this appears to be because there is less information used in the determination of the best fit of the line in the coarsely binned spectrum.

To determine the goodness of fit, then, we used the "goodness" procedure in XSPEC to perform many Monte Carlo simulations, between 2000 and 5000. During each simulation, a spectrum is generated from the

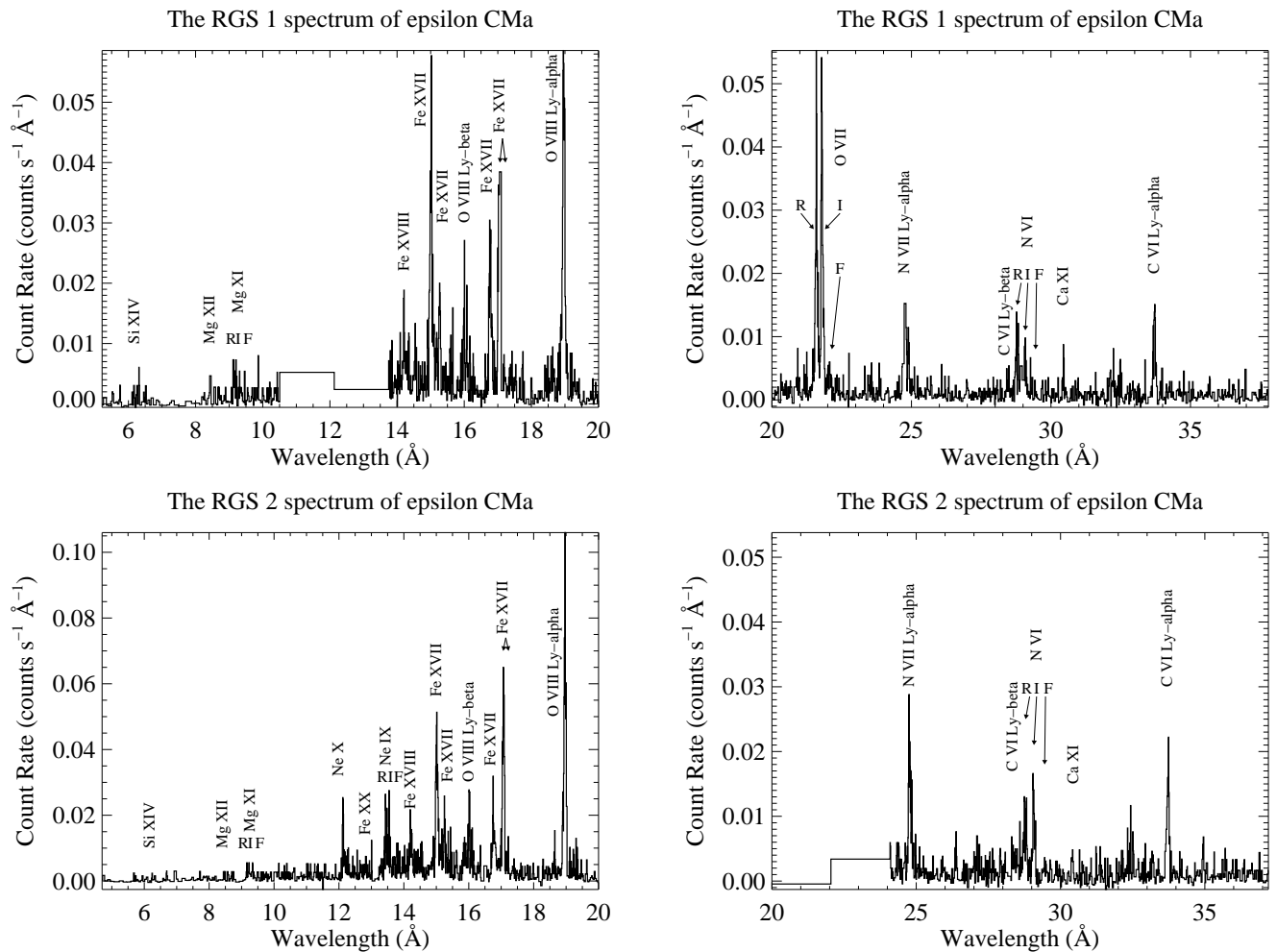


Fig. 1.— The RGS 1 and RGS 2 spectra of ϵ Canis Majoris. The RGS 1 has a gap in sensitivity between 10 and 14 Å. The RGS 2 has a gap between 20 and 25 Å.

best-fit model, using Poisson errors, and the model's fit statistic on the generated spectrum is compared to the fit statistic on the real spectrum. The percentage of generated spectra which have a lower fit statistic is noted, so a low percentage indicates that the model is a good fit.

A few notes on the uncertainties of a Gaussian fit:

To model an emission line against continuum, we combined a Gaussian and a bremsstrahlung model. If the continuum was particularly low, we left out the bremsstrahlung term. To model a series of emission lines, we combined several Gaussians with a bremsstrahlung. We loosely confined the range of temperatures allowed for the bremsstrahlung, but allowed the bremsstrahlung model to vary from fit to fit because it is generally so weak that we could not determine its specific characteristics.

The parameters we are interested in are the position, width and amplitude of the Gaussian model, and the temperature and amplitude of the bremsstrahlung model. To determine confidence intervals, we calculated the shape of the first, 68% confidence interval in two-dimensional parameter space: first position and width, then position and amplitude. It should be noted that the steppar procedure varies all parameters, even when asked to vary two parameters across a specified range. Therefore, in the case where position and width were the parameters of interest, the amplitude was still not frozen at its best fit value. After finding the shape of the first confidence interval, we measured its lower and upper bounds in both directions and recorded the difference from the best fit.

We typically confined the range of data to be considered closely around the emission line, to avoid artificially narrowing the confidence region. The information is contained within the narrow range of the emission line. If a broad range of low continuum is considered in the fit, the significance of the data in the line is de-emphasized, and the confidence region may decrease compared to an otherwise identical fit across a narrow region.

4.2. Line fits

4.2.1. Line width diagnostic

The width of an emission line is resolved only if it is not much narrower than the instrumental broadening of the telescope. If the signal to noise is very high, an emission line with about half the width of the instrumental broadening may be resolved. The HWHM instrumental broadening of the RGS in the relevant area of the spectrum is about 0.03 \AA , or 450 km s^{-1} at 20 \AA (see Section 3.1). Compared to this, the effects of the rotation of the star and thermal broadening at the expected temperatures are undetectable. The rotation of the star is very slow: $V \sin i = 25 \text{ km s}^{-1}$. The rms thermal velocity is given by

$$v_{\text{therm}} = \sqrt{\frac{3kT}{m}} \quad (1)$$

We found that the average temperature in the plasma was about 0.16 keV (see Section 4.3) = 1.86 MK . Then the thermal broadening is 54 km s^{-1} for oxygen, and 29 km s^{-1} for iron.

To correct for these two types of broadening when finding upper bounds on the wind speed, we subtract the rotational and thermal broadening from the total broadening, in quadrature:

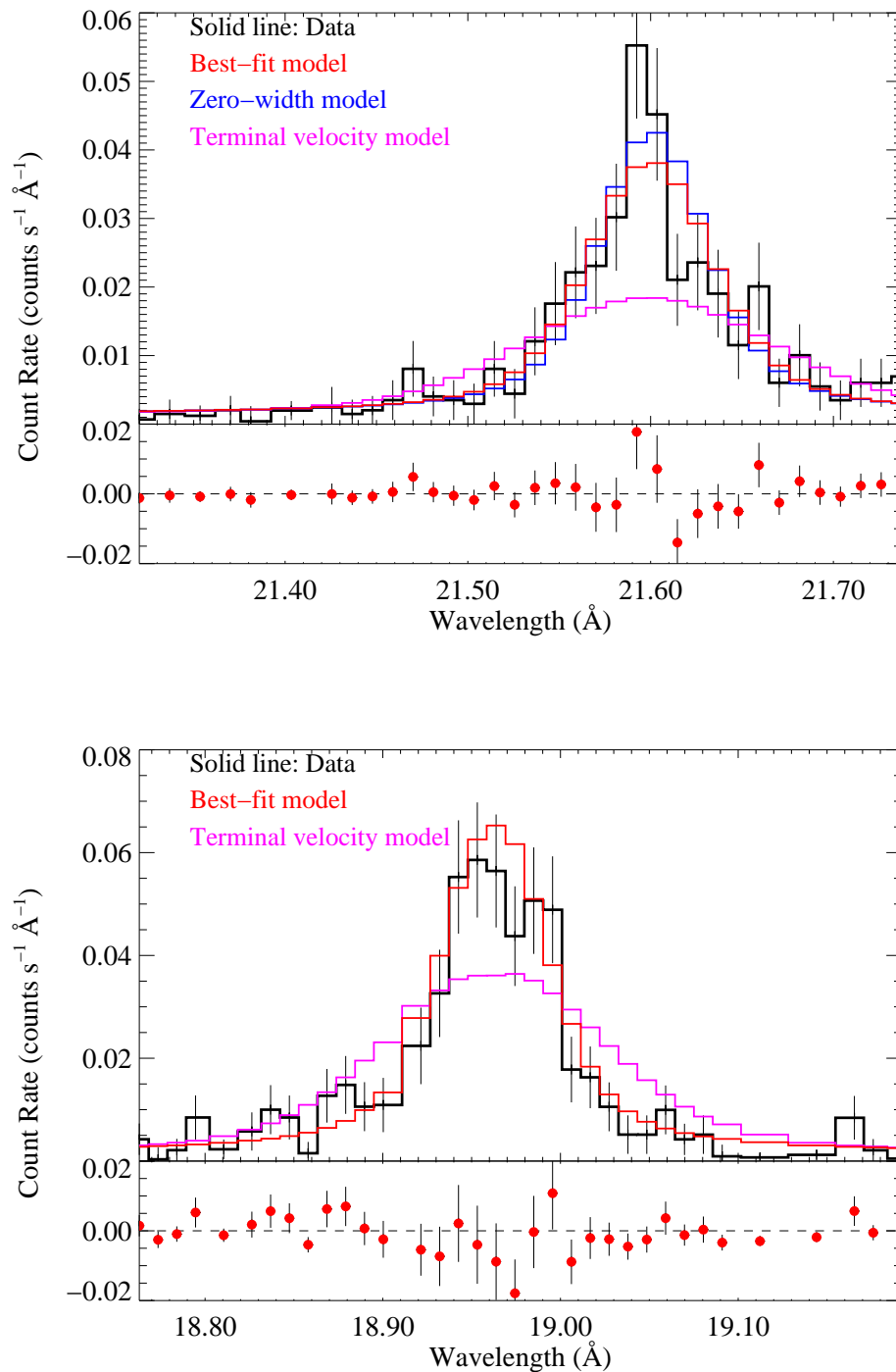


Fig. 2.— The O VII resonance line and the O VIII Lyman- α line, with best fit models. The zero width model fits the O VII line to within one significance level, and the O VIII line was found to be intrinsically narrow. The terminal velocity model does not fit the data for either line well.

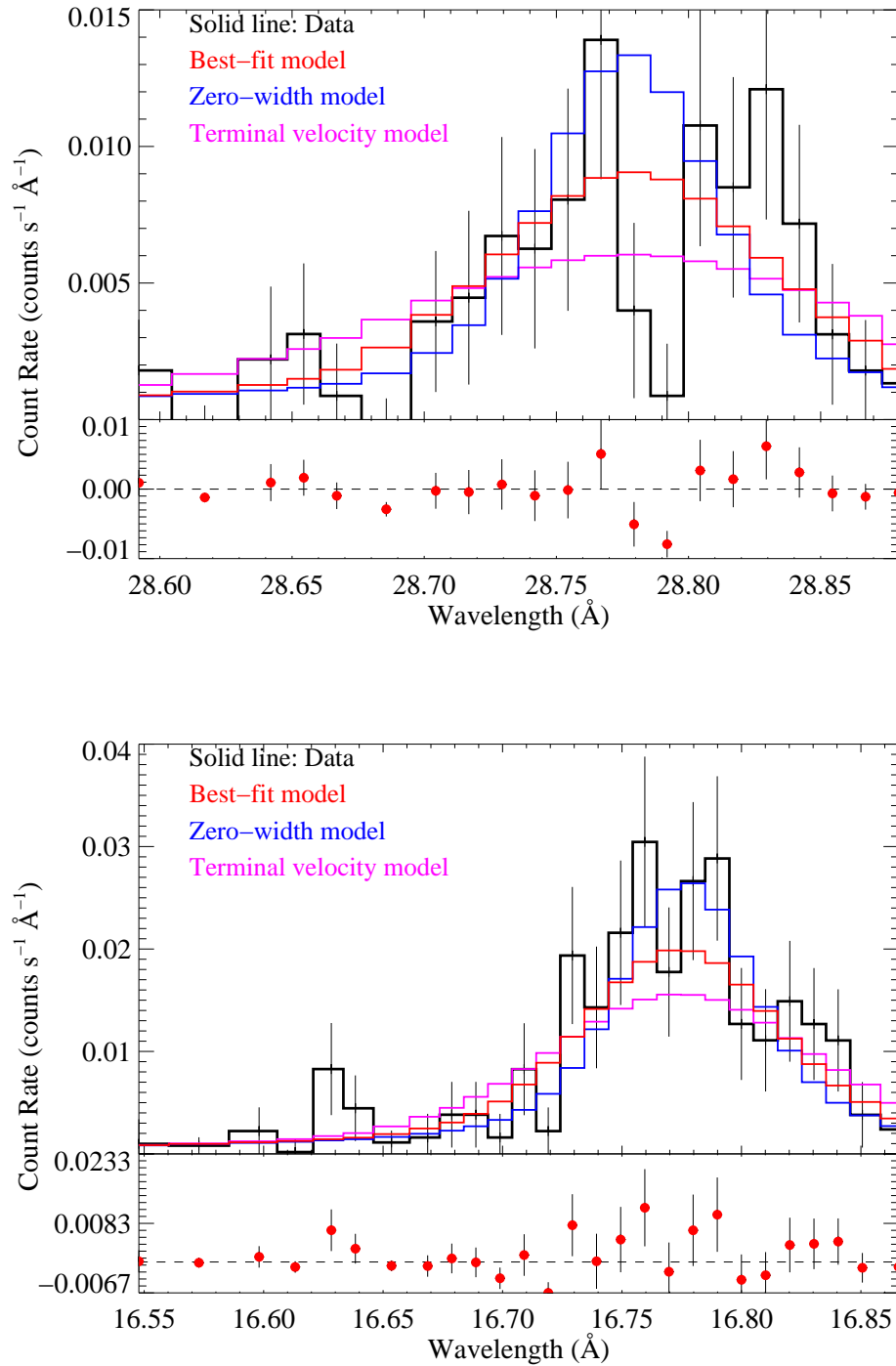


Fig. 3.— The N VI resonance line and the Fe XVII line at 16.78 Å, with best fit models. These lines have intermediate width. Neither the zero width model nor the terminal velocity model fit the data within one significance level.

Table 2. Observation log

| Obs ID | Instrument | Order | Length (s) |
|----------|------------|-------|------------|
| 69750101 | RGS1 | 1 | 47013 |
| | | 2 | 47013 |
| | RGS2 | 1 | 47010 |
| | | 2 | 47010 |
| | EMOS1 | | 46389 |
| | EMOS2 | | 46389 |
| EPN | | 45600 | |
| 69750201 | RGS1 | 1 | 8816 |
| | | 2 | 8816 |
| | RGS2 | 1 | 8818 |
| | | 2 | 8818 |

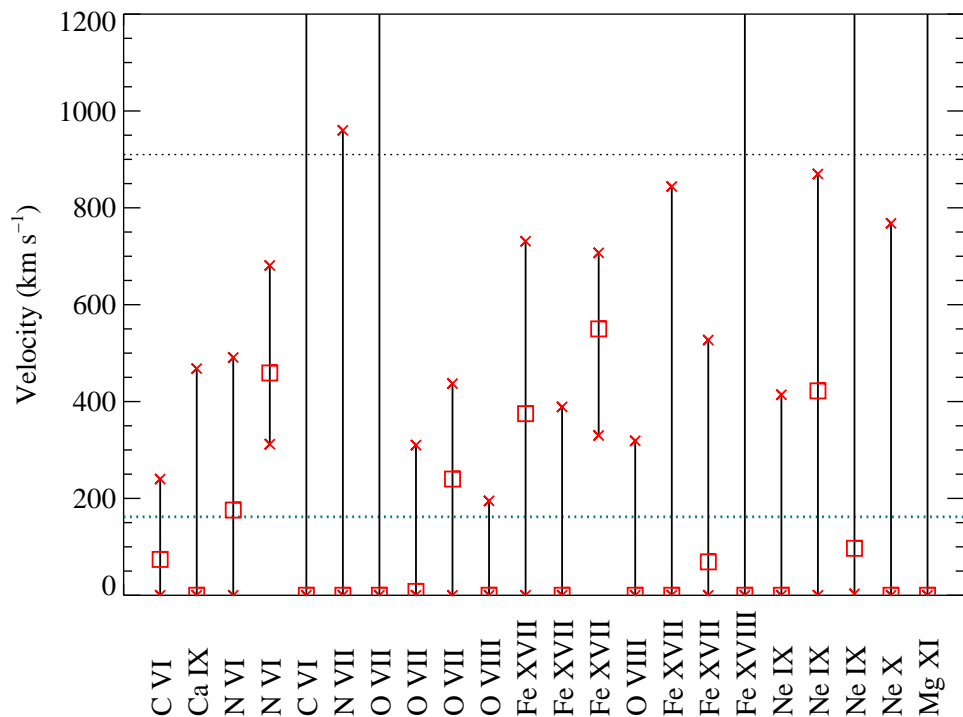


Fig. 4.— HWHM velocities for each ion, with uncertainties. The terminal velocity is at 910 km s^{-1} ; the weighted mean wind speed is 162 km s^{-1} .

Table 3. Line list

| Ion | λ_{lab} (Å) | λ_{obs} (Å) | WHHM ^a (km s ⁻¹) | F (10 ⁻⁵ ph cm ⁻² s ⁻¹) | log $T_{\text{max emiss}}$ ^b (K) |
|----------|-------------------------------|--|--|--|--|
| Si XIV | 6.180 | 6.165 ^{+1.4} _{-2.8} | 20 ₋₂₀ | 0.9 ⁺³²³⁰ _{-0.9} | 7.2 |
| Mg XII | 8.419 | 8.474 ^{+0.036} _{-0.032} | 0 | 0.7 ^{+0.4} _{-0.3} | 7.0 |
| Mg XI | 9.169 | 9.170 | 0 ⁺³³⁴⁴ ₋₀ | 0.6 ^{+0.9} _{-0.2} | 6.8 |
| Mg XI | 9.231 | 9.232 ^{+0.028} _{-0.021} | 0 | 1.0 ^{+0.7} _{-0.3} | 6.8 |
| Mg XI | 9.314 | 9.315 ^{+0.056} _{-0.014} | 0 | 1.1 ^{+0.7} _{-0.5} | 6.8 |
| Ne X | 12.134 | 12.143 ^{+0.017} _{-0.019} | 0 ⁺⁷⁶⁸ ₋₀ | 5.0 ^{+1.6} _{-2.7} | 6.8 |
| Fe XX | 12.823 | 12.823 | 0 | 1.5 ^{+0.5} _{-0.5} | 7.0 |
| Ne IX | 13.447 | 13.443 ^{+0.012} _{-0.002} | 0 ⁺⁴¹⁴ ₋₀ | 3.6 ^{+1.0} _{-0.5} | 6.6 |
| Ne IX | 13.553 | 13.550 ^{+0.014} _{-0.010} | 422 ⁺⁴⁴⁸ ₋₄₂₂ | 2.5 ^{+0.6} _{-0.6} | 6.6 |
| Ne IX | 13.698 | 13.687 ^{+0.047} _{-0.022} | 97 ⁺¹⁷⁰⁰ ₋₉₇ | 0.7 ^{+0.4} _{-0.3} | 6.6 |
| Fe XVIII | 14.208 | 14.198 ^{+0.117} _{-0.002} | 0 ⁺²⁸³⁰ ₋₀ | 2.5 ^{+4.5} _{-0.3} | 6.9 |
| Fe XVII | 15.014 | 15.013 ^{+0.006} _{-0.005} | 69 ⁺⁴⁵⁸ ₋₆₉ | 8.7 ^{+1.8} _{-0.7} | 6.7 |
| Fe XVII | 15.261 | 15.269 ^{+0.004} _{-0.015} | 0 ⁺⁸⁴⁴ ₋₀ | 3.5 ^{+1.1} _{-1.3} | 6.7 |
| O VIII | 16.006 | 16.008 ^{+0.008} _{-0.009} | 0 ⁺³¹⁹ ₋₀ | 3.0 ^{+0.8} _{-0.3} | 6.5 |
| Fe XVII | 16.780 | 16.775 ^{+0.005} _{-0.008} | 550 ⁺¹⁵⁸ ₋₂₂₀ | 5.6 ^{+0.8} _{-0.4} | 6.7 |
| Fe XVII | 17.051 | 17.051 | 0 ⁺³⁸⁹ ₋₀ | 6.8 ^{+1.6} _{-1.3} | 6.7 |
| Fe XVII | 17.096 | 17.096 | 375 ⁺³⁵⁶ ₋₃₇₅ | 5.2 ^{+1.9} _{-1.9} | 6.7 |
| O VIII | 18.969 | 18.963 ^{+0.004} _{-0.004} | 0 ⁺¹⁹⁵ ₋₀ | 14.3 ^{+0.9} _{-0.8} | 6.5 |
| O VII | 21.602 | 21.599 ^{+0.005} _{-0.008} | 240 ⁺¹⁹⁷ ₋₂₄₀ | 10.0 ^{+1.9} _{-1.4} | 6.3 |
| O VII | 21.804 | 21.793 ^{+0.007} _{-0.003} | 8 ⁺³⁰² ₋₈ | 10.9 ^{+1.6} _{-1.6} | 6.3 |
| O VII | 22.100 | 22.084 ^{+0.026} _{-0.086} | 0 ⁺¹⁶⁴⁰ ₋₀ | 1.0 ^{+0.6} _{-0.3} | 6.3 |
| N VII | 24.781 | 24.781 ^{+0.020} _{-0.021} | 0 ⁺⁹⁶⁰ ₋₀ | 7.0 ^{+0.9} _{-4.3} | 6.3 |
| C VI | 28.465 | 28.495 ^{+0.020} _{-0.167} | 0 ⁺¹⁶³⁰ ₋₀ | 1.0 ^{+1.6} _{-0.3} | 6.2 |
| N VI | 28.787 | 28.779 ^{+0.011} _{-0.011} | 459 ⁺²²² ₋₁₄₇ | 4.1 ^{+0.7} _{-0.6} | 6.2 |
| N VI | 29.084 | 29.069 ^{+0.009} _{-0.012} | 176 ⁺³¹⁵ ₋₁₇₆ | 3.5 ^{+1.0} _{-0.7} | 6.1 |
| N VI | 29.535 | 29.535 | 269 ₋₂₆₉ | 0.6 ^{+0.5} _{-0.4} | 6.1 |
| Ca XI | 30.471 | 30.425 ^{+0.022} _{-0.016} | 0 ⁺⁴⁶⁸ ₋₀ | 1.0 ^{+0.7} _{-0.3} | 6.3 |
| C VI | 33.734 | 33.718 ^{+0.006} _{-0.007} | 74 ⁺¹⁶⁶ ₋₇₄ | 6.5 ^{+1.1} _{-0.7} | 6.1 |

^aWhere uncertainties are not given, the parameter was frozen.

^bTemperature of maximum emissivity, from APED.

$$v_{\text{wind}} = \sqrt{v_{\text{total}}^2 - v_{\text{rot}}^2 - v_{\text{therm}}^2} \quad (2)$$

For all lines, we found that $v_{\text{wind}} = v_{\text{total}}$ within 5 km s^{-1} ; the thermal and rotational velocities are not significant. Therefore, we assume that all line broadening is due to a radially moving source, such as a heated stellar wind. The thermal and rotational velocities still do not have a significant effect on cases where the emission lines were fit to be intrinsically narrow, because v_{rot} and v_{therm} are much less than the instrumental resolution across the range of wavelengths.

In Figures 2 and 3, the spectrum for each of four emission lines is represented by a black line. Our best fit curve is shown in red. For comparison, we also plotted a fit with the width frozen at zero, and a fit with width frozen to the terminal velocity of $\epsilon \text{ CMa}$, 910 km s^{-1} . The oxygen lines are representative of most of the emission lines in the spectrum, which are consistent with a width of zero within one significance level. The widths of the nitrogen and iron lines are not consistent with either zero or the terminal velocity within one significance level.

The best fit width of all the emission lines ranged from 0 to 550 km s^{-1} (see Figure 4). We found the mean wind speed by averaging the widths for each emission line, weighted by upper bound:

$$\bar{v} = \frac{\sum_i \frac{v_i}{\sigma_{i,\text{upper}}^2}}{\sum_i \frac{1}{\sigma_{i,\text{upper}}^2}} = 162 \text{ km s}^{-1} \quad (3)$$

Flat-topped emission line profiles

In general, a stellar wind can be described by the β -velocity law, where β characterizes how quickly the wind accelerates.

$$v = v_{\infty}(1 - R_*/R)^{\beta} \quad (4)$$

A spherically symmetric wind has a flat-topped line profile (Figure 5) under the following assumptions: it is optically thin, emission has an inner limit, taken to be $R_{\text{min}} \approx 1.5R_*$ based on numerical simulations, and occultation by the star is neglected (Owocki & Cohen 2001).

$$\frac{dL}{d\lambda} = \eta 2\pi R^2 \Delta R \frac{c}{\lambda_o v_{\text{shell}}} = \text{constant on } \frac{-\lambda_o v_{\text{shell}}}{c} < \lambda - \lambda_o < \frac{\lambda_o v_{\text{shell}}}{c} \quad (5)$$

$$\frac{dL}{d\lambda} = 0 \text{ otherwise}$$

Note that the emissivity depends on radius:

$$\eta = \eta_o \rho^2 = \eta_o \left(\frac{\dot{M}}{4\pi R^2 v_{\text{shell}}} \right)^2 = \eta_o \left(\frac{\dot{M}}{4\pi R^2 v_{\infty} (1 - R_*/R)^{\beta}} \right)^2 \quad (6)$$

Then the profile of each shell is a step function given by

$$L_{\text{shell}} = \frac{\eta_o \dot{M}^2 c}{8\pi \lambda_o v_\infty^3} \frac{1}{R^2 (1 - R_*/R)^{3\beta}} = \text{constant on } \frac{-\lambda_o v_{\text{shell}}}{c} < \lambda - \lambda_o < \frac{\lambda_o v_{\text{shell}}}{c} \quad (7)$$

$$L_{\text{shell}} = 0 \text{ otherwise}$$

The total luminosity of the wind as a function of wavelength, λ , is obtained from integrating L_{shell} over all shells that give off light at λ . The innermost shell that is luminous at λ has width exactly equal to $\lambda - \lambda_o$, such that

$$\lambda - \lambda_o = \frac{\lambda_o v_{\text{shell}}}{c} = \frac{\lambda_o v_\infty}{c} \left(1 - \frac{R_*}{R}\right)^\beta \quad (8)$$

All shells within this one are dark at λ , by Equation 7. However, all larger shells contribute to the luminosity at λ . Therefore, $L(\lambda)$ is equal to the integral of L_{shell} over radius from a lower limit, R_{low} , to infinity.

Solving for R, the shell with width equal to $\lambda - \lambda_o$ has radius

$$R_{\text{inner shell}} = R_* \left(1 - \left(\frac{(\lambda - \lambda_o)c}{\lambda_o v_\infty}\right)^{1/\beta}\right)^{-1} \quad (9)$$

This value is equal to the lower bound of integration except for the center region of the emission line, for wavelengths such that $R_{\text{inner shell}} < R_{\text{min}}$. Nothing within R_{min} is luminous, so R_{min} is the limit of integration for the line center. Then, the profile has a flat top, and R_{low} is the maximum of R_{min} and $R_{\text{inner shell}}$.

$$L(\lambda) = \int_{R_{\text{low}}}^{\infty} L_{\text{shell}} dR \quad (10)$$

On the wings of the emission line, $R_{\text{low}} = R_{\text{inner shell}}$ and

$$L(\lambda) = \frac{\eta_o \dot{M}^2 c}{8\pi \lambda_o v_\infty^3 R_* (1 - 3\beta)} \left[1 - \left(\frac{(\lambda - \lambda_o)c}{\lambda_o v_\infty}\right)^{1/\beta - 3}\right] \quad (11)$$

At the line center, $R_{\text{low}} = R_{\text{min}}$ and

$$L(\lambda) = \frac{\eta_o \dot{M}^2 c}{8\pi \lambda_o v_\infty^3 R_* (1 - 3\beta)} \left[1 - \left(1 - \frac{R_*}{R_{\text{min}}}\right)^{1 - 3\beta}\right] \quad (12)$$

The two functions meet at the cusped edge of the profile (see Figure 5), where

$$\left(\frac{(\lambda_a - \lambda_o)c}{\lambda_o v_\infty}\right)^{1/\beta} = 1 - \frac{R_*}{R_{\text{min}}}$$

$$\lambda_a = \frac{\lambda_o v_\infty}{c} \left(1 - \frac{R_*}{R_{\text{min}}}\right)^\beta + \lambda_o \quad (13)$$

In the wavelength range $|\lambda - \lambda_o| < |\lambda_a - \lambda_o|$, L is constant.

Clearly, the dependence of $L(\lambda)$ on $\lambda - \lambda_o$ must yield a profile that is peaked toward the center, rather than increasing as $\lambda - \lambda_o$ increases. Then the exponent in both equations for $L(\lambda)$ must be negative. It follows that $\beta > 1/3$. Then the quantity $1 - \left(\frac{(\lambda - \lambda_o)c}{\lambda_o v_\infty}\right)^{1/\beta - 3} < 0$, but the negative sign is canceled out by the negative sign of the factor $1 - 3\beta$, so the line profile is positive.

Constraining β and R_{\min}

The acceleration of a stellar wind is described by β . We can put constraints on β for the hot component of the stellar wind in ϵ CMa by applying the observed velocity v_{HWHM} of a line of wavelength λ_o to the line profile equation.

$$v_{\text{HWHM}} = (\lambda_{\text{HWHM}} - \lambda_o) \frac{c}{\lambda_o} \quad (14)$$

By definition,

$$L(\lambda_{\text{HWHM}}) = 0.5L(\lambda_o) \quad (15)$$

To find $L(\lambda_o)$, we evaluate the line profile in its constant range. The constants cancel out.

$$\left[1 - \left(\frac{(\lambda_{\text{HWHM}} - \lambda_o)c}{\lambda_o v_\infty}\right)^{1/\beta - 3}\right] = \frac{1}{2} \left[1 - \left(1 - \frac{R_*}{R_{\min}}\right)^{1 - 3\beta}\right]$$

Substituting in for v_{HWHM} , we eliminate dependence on λ_o . The average wind speed is $v_{\text{HWHM}} = 162 \text{ km s}^{-1}$.

$$\left(\frac{v_{\text{HWHM}}}{v_\infty}\right)^{\frac{1}{\beta} - 3} = \left(1 - \frac{R_*}{R_{\min}}\right)^{1 - 3\beta} + \frac{1}{2} \quad (16)$$

The unknowns are R_{\min} and β . Given a reasonable value of R_{\min} , this formula constrains β , and vice versa (see Figure 6). If ϵ CMa has $\beta = 0.8$, the typical value for hot stars (Lamers & Cassinelli 1999), the inner radius of emission is $1.13R_*$, almost on the surface of the star.

4.2.2. Helium-like F/I ratio diagnostic

Background on helium-like line diagnostics

A helium-like triplet is composed of three emission lines, closely spaced in energy (Porquet et al. 2001). The resonance line is created by a spontaneous decay from the $^1\text{P}_1$ state to the ground state, $^1\text{S}_0$. The intercombination line results from the transition from either of two microstates, $^3\text{P}_1$ or $^3\text{P}_2$, down to the ground state. These two lines blend to form the intercombination line. The decay from the $^3\text{S}_1$ state to the ground state forms the forbidden line (see Figure 7).

The ratio of the strengths of the forbidden and intercombination lines yields information about how far above the surface of the star emission of X-rays occurs. $^3\text{S}_1$ is a metastable state, which gives the

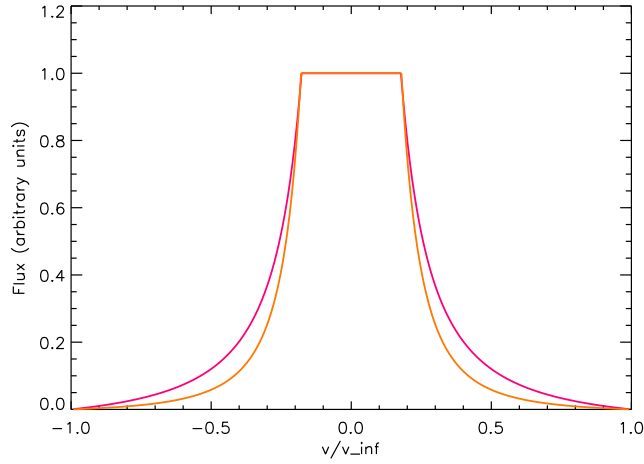


Fig. 5.— A flat-topped emission line profile, using values that satisfy Equation 16. The pink profile has $\beta = 0.8$ and $R_{\min} = 1.13$. The orange profile has $\beta=2.7$ and $R_{\min} = 2.01$. The wings of each profile are described by Equation 11, while the height of the line center is described by Equation 12. The transition wavelength λ_a between these two regimes is given by Equation 13.

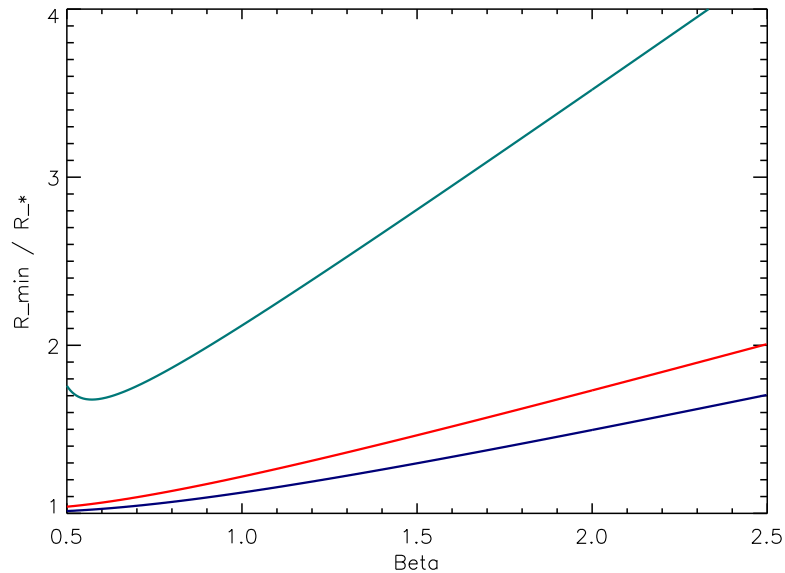


Fig. 6.— The functional dependence of β and R_{\min} , in Equation 16. $v_{\infty} = 910 \text{ km s}^{-1}$. The red line is our best fit velocity, $v_{\text{HWHM}} = 162 \text{ km s}^{-1}$. The light blue and dark blue lines are functions with $v_{\text{HWHM}} = 450$ and 100 km s^{-1} , which approximately characterize the broadest lines and a lower bound on the best fit, respectively. If wind shocks are responsible for the X-ray emission from $\epsilon \text{ CMa}$, the radius of X-ray emission must be small or the wind must accelerate slowly, or both, to explain the observed line widths.

forbidden transition its name. An electron excited to 3S_1 may not immediately spontaneously decay. The energy interval between 3S_1 and either of the 3P microstates is in the ultraviolet. If a photon with this energy is incident upon the ion during that pause, the electron may be excited to the upper level of the intercombination transition. It will then immediately decay and produce an intercombination photon, at the expense of the forbidden line.

Therefore, in the presence of a strong ultraviolet field (Porquet et al. 2001), the forbidden line of a triplet may be destroyed in favor of the intercombination line. Ordinarily, the forbidden line is two or three times as strong as the intercombination line. The nitrogen and oxygen triplets (Figure 8) are examples of nearly total destruction of the forbidden line.

By comparing the f/i ratios of several elements, we can set upper and lower bounds on the radius of X-ray emission. The forbidden line of a light element, like oxygen, can be completely destroyed even in the presence of a relatively weak ultraviolet field. If the forbidden line of magnesium or silicon is destroyed, there is a strong indication that emission must be occurring near the photosphere.

We note that the forbidden line can be destroyed in favor of the intercombination line by collisional excitation between ions and free electrons, as well as by photoexcitation. Typically, one of these two processes will be dominant in some environment. As shown below, radiative excitation is expected to dominate for ϵ CMa.

Electron densities on ϵ CMa

The electron densities around ϵ CMa are given by the expression

$$\rho(R) = \frac{\dot{M}}{4\pi R^2 v} \quad (17)$$

Using the β -velocity law with $\beta = 0.8$,

$$\rho(R) = \frac{\dot{M}}{4\pi R^2 v_\infty (1 - R_*/R)^\beta} \quad (18)$$

We enter the values of \dot{M} , R_* , and v_∞ quoted in Table 1, and let the mean molecular weight $\bar{\mu} = 1.2$. Then the number density is

$$n = \frac{\rho}{m_H \bar{\mu}} = \frac{4.5 \times 10^8}{(R/R_*)^2 (1 - R_*/R)^{0.8}} \text{ cm}^{-3} \quad (19)$$

To correct for the discontinuity at the surface of the star, note that the velocity at the surface of the star should be a small positive minimum. These densities are low. However, the peak radiation of a 20990 K blackbody is at 1380 Å (Wien's Law), in the ultraviolet. Therefore, we expect UV flux to be strong, and photoexcitation to be the dominant process.

Fitting the helium-like triplets

Our best fit models for the helium-like triplets are shown in Figure 8 and Figure 9. The resonance lines are at the shortest wavelength; the forbidden lines are at the longest.

The nitrogen triplet was fit using several different spectra: both the resonance and intercombination lines were fit using the first orders of both RGS instruments of the longer observation. The intercombination

line was also fit using the same spectra from the shorter observation, for a total of four spectra. The forbidden line was fit using only the first order from the RGS 2 instrument from the longer observation. This spectrum is the one shown in Figure 8 for all three lines, with the corresponding models shown in red, orange and pink. A bremsstrahlung model was simultaneously fitted for the continuum for the resonance and intercombination lines, but not for the weaker forbidden line.

The intercombination and resonance lines of the oxygen triplet were fit using the first order of the RGS 1 instrument for both observations. Only the longer observation was used to fit the forbidden line because it is a weaker line (see Section 3). The data shown in Figure 8 is from the longer observation for all of the lines. A bremsstrahlung model was used for all three fits.

The lines of the neon triplet were fitted simultaneously because the line wings are blended. The spectra used were the first order of the RGS 2 instrument and the second order of the RGS 1 instrument, both from the longer observation. The first order spectrum has stronger signal-to-noise and is the spectrum plotted in Figure 9, with the model in red. A bremsstrahlung model was included.

The magnesium triplet is near the edge of the sensitivity of the RGS, and the signal to noise is lower. The resonance and intercombination lines, shown in red and orange in Figure 9, were modeled with the first order of the RGS 2 instrument in the longer observation. The forbidden line was fitted using the second order of the same instrument, and is shown in pink. A bremsstrahlung continuum was included in the fit for the intercombination and resonance lines.

The resulting f/i ratios are listed in Table 4. The forbidden line of magnesium has undergone some destruction but is still strong. The neon forbidden line is mostly destroyed. The forbidden lines of nitrogen and oxygen have been almost completely destroyed. They are not quite consistent with zero flux, however. The nonzero lower bound turns out to have a large effect on the conclusions of this diagnostic.

There is no significant interference on either the nitrogen or oxygen forbidden lines by other lines at the plasma's temperature of emissivity. However, there may be contamination from lithium-like satellite lines of the resonance line (MacFarlane et al. 2000). When an electron in a lithium-like oxygen ion decays to produce a resonance photon, the cancellation of charge due to another electron in an elevated energy state can slightly decrease the energy of the photon. The satellite lines, thus produced, are spread out across a range of wavelengths, and they are not very strong. However, in conditions of low temperature, around 0.5 MK, the flux of the satellite lines near the helium-like forbidden line can be of order unity with the forbidden line.

There may be a large amount of plasma at these cool temperatures around ϵ CMa (see Section 4.3). Furthermore, an examination of the spectrum near the laboratory wavelength of the forbidden lines (see Figure 8) shows that the features in question are broad, without a well defined emission line profile. The forbidden lines of nitrogen and oxygen may be completely destroyed after all. For the purposes of analyzing the f/i ratios, we set a lower bound of zero on the flux.

Radius of emission implied by f/i ratios

The amount of destruction of the forbidden line, whether caused by collisional or radiative excitation, depends on the dilution factor W , which describes how much of the sky is subtended by the star at some radius:

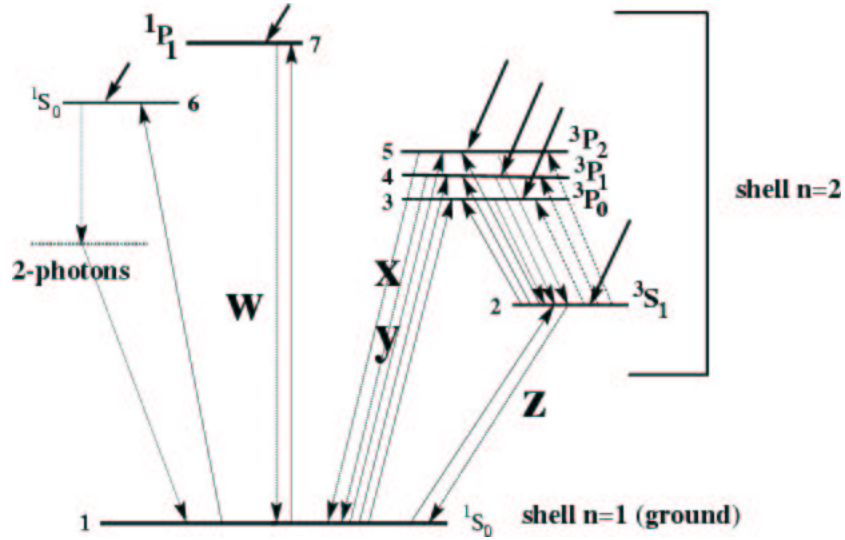


Fig. 7.— Energy transitions of helium-like ions (Porquet et al. 2001). The resonance line is denoted by w , the intercombination line by x and y , and the forbidden line by z .

Table 4. F/I Ratios

| Ion | F/I Ratio |
|-------|-------------------------------------|
| N VI | $0.17^{+0.19}_{-0.13}$ ^a |
| O VII | $0.09^{+0.06}_{-0.03}$ ^a |
| Ne IX | $0.29^{+0.17}_{-0.14}$ |
| Mg XI | $1.08^{+0.77}_{-0.91}$ |

^aNote that while we fit a Gaussian model with a nonzero lower bound, plausibility arguments related to the presence of lithium-like satellite line emission show that the lower bound on this flux should be zero.

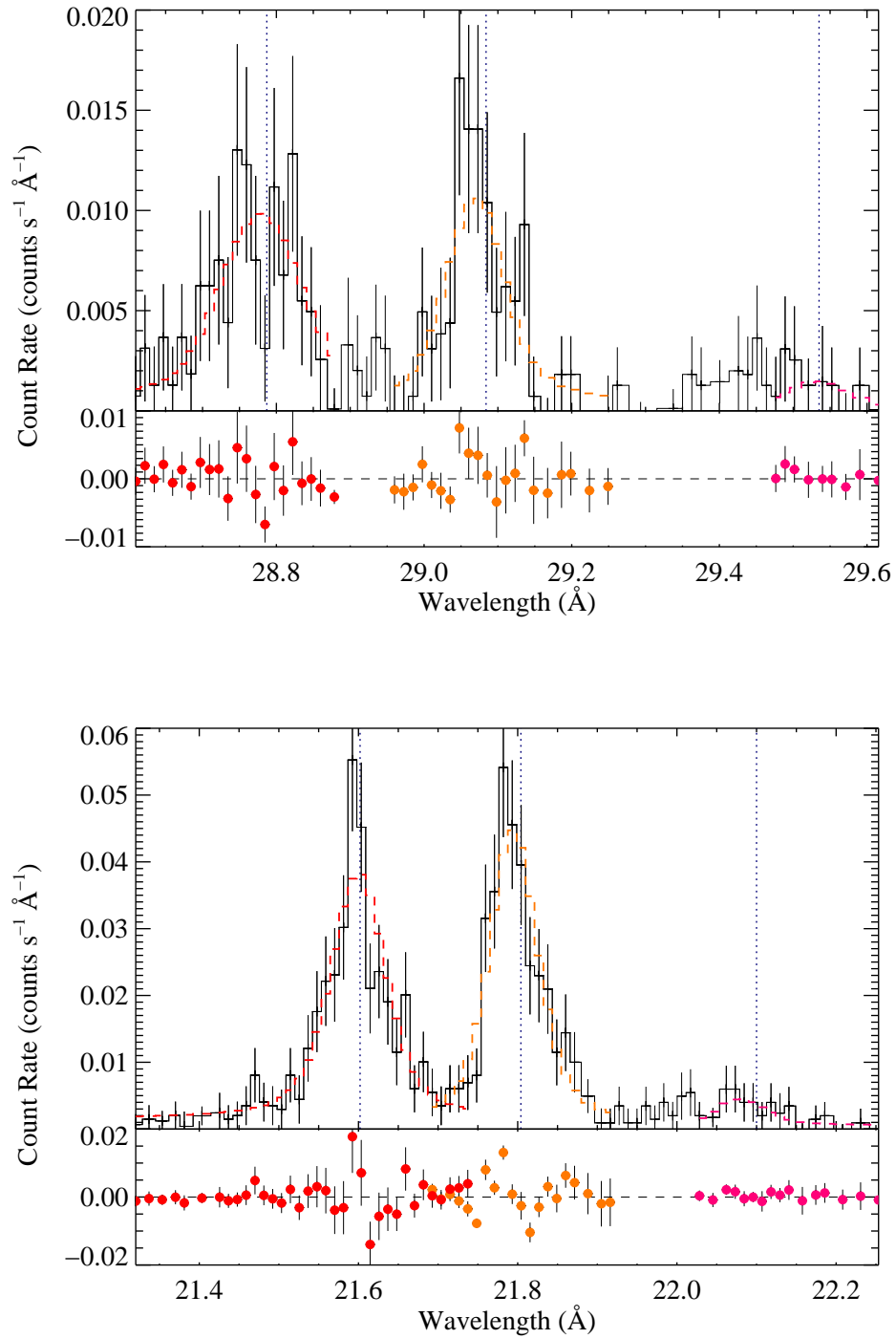


Fig. 8.— Helium-like triplets: N VI and O VII. Blue dotted lines indicate laboratory line centers.

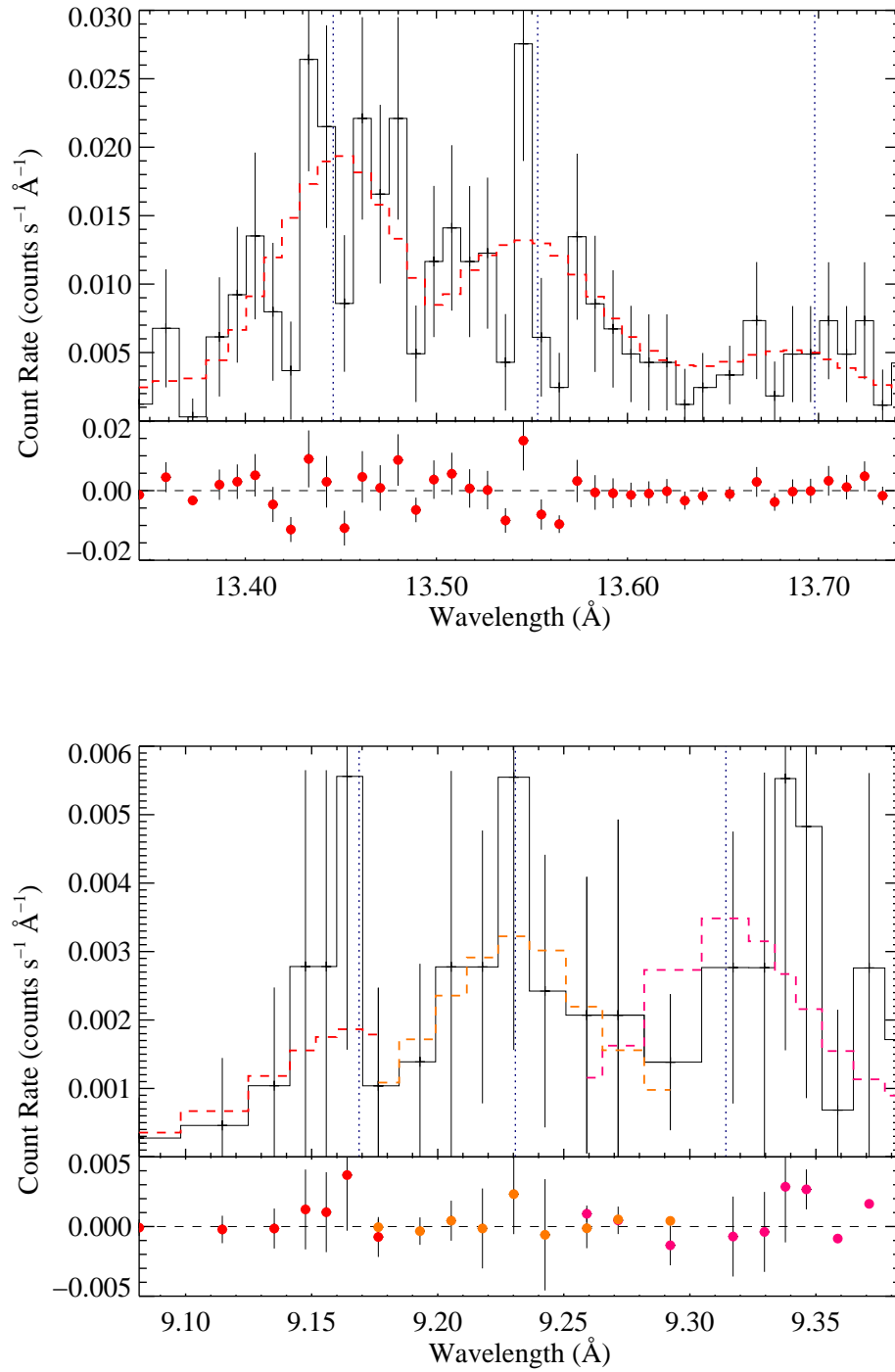


Fig. 9.— Helium-like triplets: Ne IX and Mg XI. Blue dotted lines indicate laboratory line centers.

$$W = \frac{\Omega_{\text{source}}}{4\pi} = 0.5 \left(1 - \sqrt{1 - \frac{R_*}{R}} \right) \quad (20)$$

Then W is equal to 0.5 at the surface of the star, where the source occupies half of the sky, and diminishes at large radii. If the X-ray-emitting plasma is close to the surface of the star, near $W = 0.5$, the f/i ratio should be low compared to the ratio for the same ion at a radius where the dilution factor is small.

Porquet et al (2001) produced tables with calculated f/i ratios for each helium-like ion, given the star's effective temperature, T_{rad} , and the dilution factor, W . The results also depend on electron density, n_e , and plasma temperature, T_e . However, we assume low density, and used the lowest density available for each ion in the tables. In addition, the results are only weakly dependent on plasma temperature. The reason is that the number of electrons in an excited state depends on the energy of that state, relative to the ground state, and on the temperature. The intercombination and forbidden lines have such similar energies that changing the temperature has little effect on the f/i ratio. We use the temperature of maximum emissivity for each ion.

From Table 5, it is clear that for an early-type B star, the nitrogen and oxygen forbidden lines will be completely destroyed in the stellar photosphere. In fact, they will experience severe destruction even at large radii. However, the energy interval between the 3S_1 state and the 3P microstates is larger for a heavier ion like magnesium. Ultraviolet light at shorter wavelengths is required to excite electrons out of the upper level of the forbidden transition into the upper level of the intercombination transition. The Planck function drops off steeply at wavelengths shorter than the peak, so the abundance of light with energy high enough to destroy the forbidden line of magnesium is lower. The forbidden line of magnesium will be only partially destroyed even in the photosphere. Therefore, our calculated f/i ratios for these four ions should yield a good constraint on the radius of X-ray emission.

To find the radius of emission corresponding to these ratios, it is necessary to interpolate on the theoretical data points. A logarithmic fit was the most appropriate for all of the ions, though the fit was only slightly better than a linear fit for magnesium (see Figure 10).

Each interpolation yields a range of radii of emission that are consistent with the measured f/i ratios. The best fit value of the f/i ratio for nitrogen suggests virtually infinite radius of emission, because the ratio is nonzero. The lower bound is a radius of $1R_*$, however, so the nitrogen triplet does not constrain the radius of emission at all. The oxygen ratio implies a radius of $9.2_{-8.2}^{+37.7} R_*$. The neon indicates $1.4_{-0.3}^{+0.7} R_*$. For magnesium, the result is $1.0_{-0.0}^{+4.0}$. Clearly, the radius of emission is no less than $1 R_*$, so the lower bounds of nitrogen, oxygen, and magnesium are set to this value. The lower bound of neon is just slightly above $1R_*$. All of the f/i ratios are consistent with a radius of X-ray emission within $0.6R_*$ of the photosphere.

4.3. Global fits

A global temperature fit is made to the entire spectrum at once, and predicts the strength of each emission line and the shape of the continuum based on plasma temperature. We found that the APEC temperature model fit the spectrum of ϵ CMa well. The position and width of the theoretical emission lines were in good agreement with the data.

However, when we attempted to characterize the spectrum with a single temperature fit, we found that the model has a tendency to overestimate or underestimate line strengths. A two-temperature APEC model

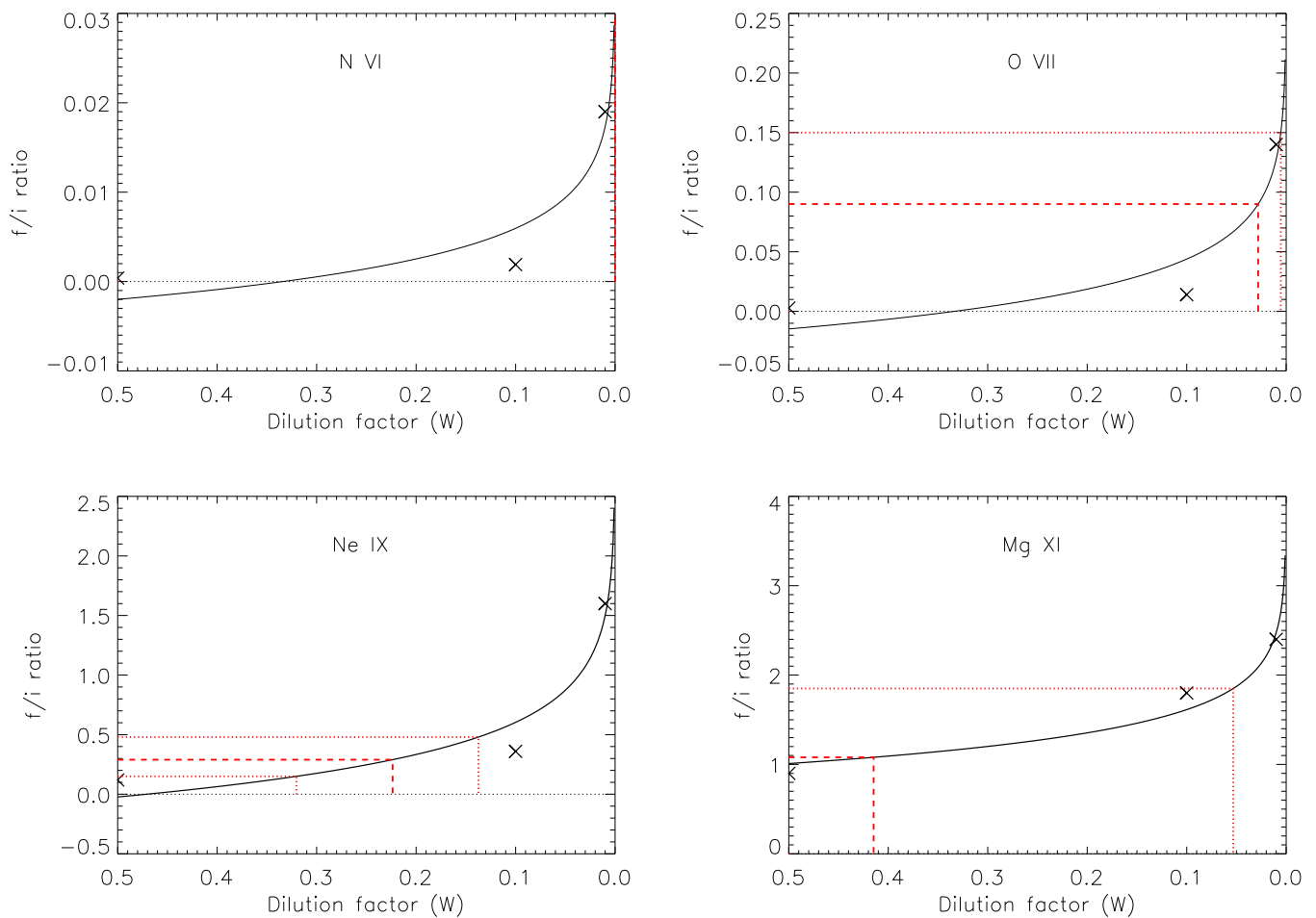


Fig. 10.— The implications of the f/i ratios on radius of emission. The data points and black curves represent the theoretical model (Porquet et al. 2001). The red dashed lines show the f/i ratio observed on ϵ CMa, and the corresponding dilution factor given by the model. The red dotted lines show the upper and lower 68% uncertainties on the f/i ratios, and the corresponding dilution factors. Note that the uncertainty on N VI and O VII spans virtually the entire range.

was able to fit the amplitudes of the lines better, though it does not account for forbidden line destruction. The two model temperatures are 0.15 and 0.49 keV, with similar amplitudes of 4.4 and 5.5, in arbitrary units of normalization.

Finally, we fit a three-temperature APEC model to the RGS1 and RGS2 first order (Table 6). The amplitude of the lowest temperature component was the largest, but it was also consistent within one significance level with 0.05 keV, corresponding to 0.6 MK, the hard lower bound we set for the temperature parameters. Therefore, the low-temperature component may describe plasma at temperatures lower than 0.6 MK. We do not expect to be able to fit cold plasma well, because the sensitivity of the RGS spectrometer drops off below the C VI line at 33.734 Å, which has a temperature of maximum emissivity of 1.3 MK. Generally, the confidence intervals on the three-temperature model are narrower than on the two-temperature model. However, the two high temperatures are the temperatures of primary interest for modeling the X-ray-emitting plasma.

It has previously been shown that the plasma temperatures near ϵ CMa are best described with a continuous temperature model, with a large fraction of cold plasma (Cohen et al. 1996). However, 0.16 and 0.49 keV can characterize the temperature distribution, especially because the temperatures of maximum emissivity used in Section 4.2.2 are described well by them.

5. Conclusions

The narrow emission lines lead to the conclusion that the X-ray-emitting material on ϵ Canis Majoris cannot be moving very quickly for any reason, whether in a shocked stellar wind moving outward, or with high thermal velocities. This result favors the coronal model, which predicts that plasma will be heated to X-ray-emitting temperatures while magnetically confined to the vicinity of the star, without significant movement outward. Nearly all of the emission lines support a model which predicts zero Doppler broadening.

However, the weighted mean line width is 162 km s^{-1} , implying that emission of X-rays can occur as close to the photosphere, but no closer than, $1.13R_*$ when $\beta = 0.8$. For larger values of β , the radius of minimum emission increases; it is $2.01R_*$ for $\beta = 2.5$. Therefore, the line widths are consistent with a slowly accelerating shocked stellar wind, located within about half of a stellar radius of the photosphere. This is closer to the star than stellar wind models typically predict (Feldmeier 1995).

The ratios of the forbidden line to the intercombination line suggest a radius of emission between 1 and $2.1 R_*$. These results are consistent with a coronal model predicting heated plasma just above the photosphere. A strong wind shock model with heated plasma at extended radii is not consistent with our results, but any wind shock model which predicts X-ray emission within one stellar radius of the photosphere does agree with these data.

The line width and f/i ratio diagnostics both support the coronal model, though both diagnostics suggest that the minimum radius of emission may be slightly greater than $1R_*$. Even tentative consistency between our data and the coronal model is interesting, because the corona of a hot star is not expected to heat plasma to X-ray-emitting temperatures. Any appreciable Doppler broadening would conflict with the observations of other late-type coronal X-ray sources. Therefore, future observations of ϵ CMa under higher resolution would be a useful test of the lower bound on the emission line widths.

If a shocked stellar wind is the source of the X-rays, its behavior is not entirely consistent with models of stellar winds on hot stars. A typical value of β for hot stars is 0.8, which on ϵ CMa implies that X-rays are

Table 5. Theoretical F/I ratios ^{a,b}

| W | N VI ^c | O VII ^d | Ne IX ^e | Mg XI ^f |
|------|-------------------|--------------------|--------------------|--------------------|
| 0.50 | 0.00039 | 0.0029 | 0.12 | 0.9 |
| 0.10 | 0.0019 | 0.014 | 0.36 | 1.8 |
| 0.01 | 0.019 | 0.14 | 1.6 | 2.4 |

^aPorquet et al. (2001)

^b $T_{\text{rad}} = 20990$ K

^c $n_e = 10^8$ cm⁻³; $T_e = 1$ MK

^d $n_e = 10^8$ cm⁻³; $T_e = 2$ MK

^e $n_e = 10^{10}$ cm⁻³; $T_e = 4$ MK

^f $n_e = 10^{12}$ cm⁻³; $T_e = 6.3$ MK

Table 6. Three-temperature APEC model

| Temperature (keV) | Normalization (arbitrary units) |
|---------------------------|------------------------------------|
| $0.054^{+0.001}_{-0.004}$ | $33.5^{+29.0}_{-9.0}$ |
| $0.156^{+0.012}_{-0.003}$ | $3.8^{+0.3}_{-0.4}$ |
| $0.490^{+0.006}_{-0.019}$ | $5.5^{+0.3}_{-0.1}$ |

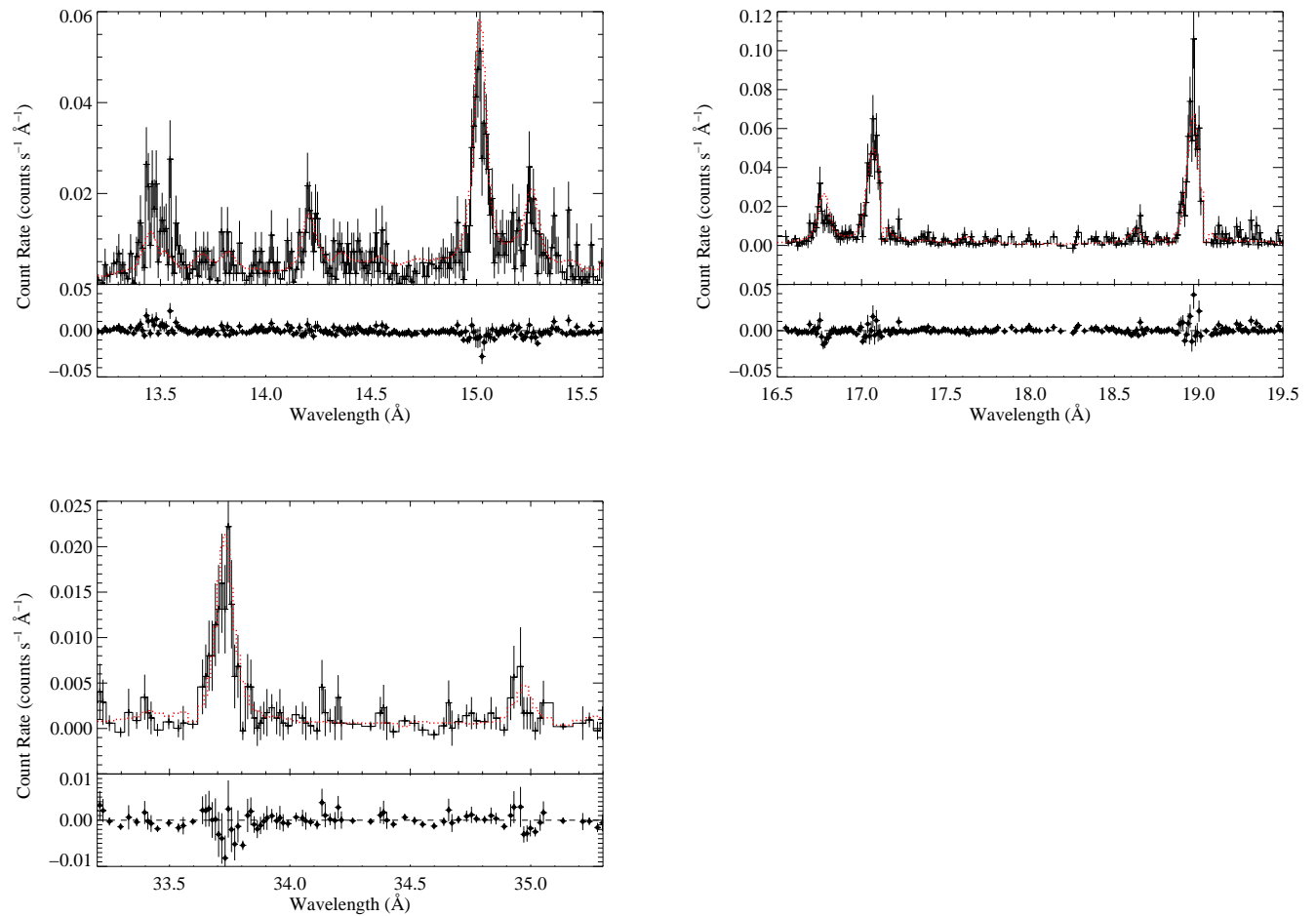


Fig. 11.— Three-temperature APEC model. The regions shown are from the RGS 2 first order spectrum. The model fits the data well, though we assume that it approximates a continuous plasma temperature distribution.

generated within $1.13R_*$. The range of X-ray emission predicted by models is about 1.5 to $7 R_*$. Therefore, if the stellar wind is accelerating quickly, it must generate shocks much closer to the surface than predicted by theory.

Our data are consistent with a higher minimum radius of emission, but it must correspond to a very slowly accelerating wind. If the minimum radius is $2.1R_*$, the value of β corresponding to the weighted mean wind velocity of 162 km s^{-1} is 2.7.

We cannot distinguish between the coronal and wind shock models for ϵ Canis Majoris. We note, however, that hot stars are not expected to be coronal X-ray sources, and that our data are consistent with moderate line broadening. If the source of X-rays is in a stellar wind, it must be close to the stellar surface, or accelerate slowly.

5.1. Acknowledgements

I would like to acknowledge Swarthmore College, Prism Computational Sciences, and the Delaware Space Grant College Scholarship for funding. My research was aided by many discussions with Eric Jensen, Chris Burns and Stan Owocki. David Cohen has been a very supportive and patient advisor.

This research has made use of the SIMBAD database, operated at CDS, Strasbourg, France.

REFERENCES

- Abt, H.A., Levato, H., & Grosso, M. 2002, ApJ, 573, 359.
- Arnaud, K.A. 1996, Astronomical Data Analysis Software and Systems V, eds Jacoby G. and Barnes J., p17, ASP Conf. Series volume 101.
- Cassinelli, J.P. et al. 1995, ApJ, 438, 932.
- Code, A.D., Davis, J., Bless, R.C., & Brown, R.H. 1975, ApJ, 203, 417.
- Cohen, D.H., Cooper, R.G., MacFarlane, J.J., Owocki, S.P., Cassinelli, J.P., & Wang, P. 1996, ApJ, 460, 506.
- Cohen, D.H., Cassinelli, J.P., & MacFarlane, J.J. ApJ, 487, 867.
- Culhane, L. 2001, in Encyclopedia of Astronomy and Astrophysics, ed. P. Murdin (Philadelphia; Institute of Physics Publishing and Nature Publishing Group), 476.
- Ehle, M. et al. 2003, "XMM-Newton User's Handbook," Issue 2.1.
- Feldmeier, A. 1995, A&A, 295, 523.
- Gregorio, A., Stalio, R., Broadfoot, L., Castelli, F., Hack, M., & Holberg, J. 2002, A&A, 383, 881.
- Gry, C. & Jenkins, E.B. 2001, A&A, 367, 617.
- Hanbury Brown, R., Davis, J., & Allen, L.R. 1974, MNRAS, 167, 121.
- Kahn, S.M. et al. 2001, A&A, 365, 312.

Kramer, R.H. 2003, Thesis, Swarthmore College.

Lamers, H.J.G.L.M., & Cassinelli, J.P. 1999, Introduction to Stellar Winds (New York, NY; Cambridge University Press).

MacFarlane, J.J, Cassinelli, J.P., Miller, N., Cohen, D.H., & Wang, P. 2000, Bulletin of the AAS, 32, 1255.

Owocki, S.P. & Cohen, D.H. 2001, ApJ, 559, 1108.

Porquet, D., Mewe, R., Dubau, J., Raassen, A.J.J., & Kaastra, J.S. 2001, A&A, 376, 1113.

Walborn, N.R. & Fitzpatrick, E.L. 1997, VizieR Online Data Catalog: III/195.